Materials Advances

ROYAL SOCIETY OF CHEMISTRY

PAPER

View Article Online
View Journal | View Issue

Cite this: *Mater. Adv.*, 2023, 4, 1101

Predicting and accessing metastable phases†

V. Kocevski, *[a] J. A. Valdez,[a] B. K. Derby,[b] Y. Q. Wang,[a] G. Pilania[a] and B. P. Uberuaga[a]

Metastable forms of matter are invaluable to our everyday lives, from advancing technology to understanding biological processes, with their unique properties often offering novel functionality. Despite their importance, synthesizing metastable phases is more art than science, often either serendipitous or trial-and-error. Insight into the amount of stored energy needed to form a metastable phase can aid in their fabrication. Here, we calculate metastable phase diagrams, from which we extract the metastability threshold – the excess energy stored in the metastable phase relative to the ground state. Using lanthanide sesquioxides (Ln_2O_3) as a case study, we demonstrate how metastable phase diagrams provide new insight into their synthesis and irradiation behavior. We successfully predict the sequence of metastable phases induced by irradiation in Lu_2O_3, forming three metastable phases with increasing irradiation fluence.

Received 20th October 2022,
Accepted 13th January 2023

DOI: 10.1039/d2ma00995a

rsc.li/materials-advances

Introduction

Gazing out through our glass windows, satisfying our sweet tooth with chocolate, or enjoying the beauty of diamonds, we encounter metastable forms of matter throughout our everyday lives. Metastable phases make our lives more convenient, but they are also necessary ingredients for all biological systems, as exemplified by the metabolic pathways responsible for cellular-level energy generation *via* the formation of metastable adenosine triphosphate molecules. A metastable phase or a molecule is a non-equilibrium state of matter, and its formation depends on the accessibility of the configuration under changes in environmental conditions (temperature, pressure, electromagnetic fields, irradiation, *etc.*), see Fig. 1a.

A group of materials having rich polymorphism with various properties shown to form metastable phases are lanthanide sesquioxides (Ln_2O_3), making them an ideal case study for understanding metastable phase formation. The relative ease with which they transform to different polymorphs enhances their ionic conductivity and amorphization resistance, making them useful for solid oxide fuel cells[1] and irradiation resistant materials.[2] Ln_2O_3s are also used as gate oxides,[3–5] ultrafast and high-power solid-state lasers,[6–9] heterogeneous catalysts,[10–12] high performance super-capacitors,[13] corrosion resistive coatings,[3,14] and in biomedical applications.[15–17] Furthermore, their functionality often depends on the formation of metastable phases; for example, the metastable phases have a much higher dielectric constant compared to the ground state phase, which makes them attractive as high-κ gate oxides.[5,18,19] To analyze the propensity of Ln_2O_3 compounds to form metastable phases, we use density functional theory (DFT) to determine the metastability threshold of all relevant phases (see Fig. 1b) and use those to generate metastable phase diagrams (see Fig. 1c). The metastable phase diagrams were ultimately used to understand the formation of metastable phases and predict which metastable phases can form at specific conditions.

As highlighted in Fig. 2a, five polymorphs of Ln_2O_3 have been reported, termed as A, B, C, H and X, with their stability depending on the temperature and pressure. At room temperature and atmospheric pressure, lanthanides with large ionic radius (La–Nd) preferably adopt a trigonal A phase, while the smaller lanthanides (Pm–Lu) adopt a cubic C phase. At intermediate temperatures (1000–2000 K), lanthanides with intermediate radius (Sm–Ho) adopt a monoclinic B phase. At high temperatures (>2000 K), the Ln_2O_3 form two disordered phases, the hexagonal H and cubic X phases, with the H phase forming at lower temperatures than the X phase. These structures are highlighted in Fig. 2b–d.

Our current knowledge of the stability of these phases and which are likely to form under non-equilibrium conditions comes from extensive experimental trial and error. One way to predict which metastable phases can form before performing experiments is to use DFT calculations. Over the years, DFT has been demonstrated to be a valuable tool that complements

[a] *Materials Science and Technology Division, Los Alamos National Laboratory, Los Alamos, NM, 87545, USA. E-mail: kocevski@lanl.gov, vancho.vk@gmail.com*
[b] *Center for Integrated Nanotechnologies, Los Alamos National Laboratory, Los Alamos, NM, 87545, USA*

† Electronic supplementary information (ESI) available: Phonon dispersions of studied polymorphs. Table containing the crystallographic parameters of the different polymorphs for all studied chemistries. Table containing the parameters used for shifting the total energies. Metastable phase diagrams of the studied chemistries. See DOI: https://doi.org/10.1039/d2ma00995a

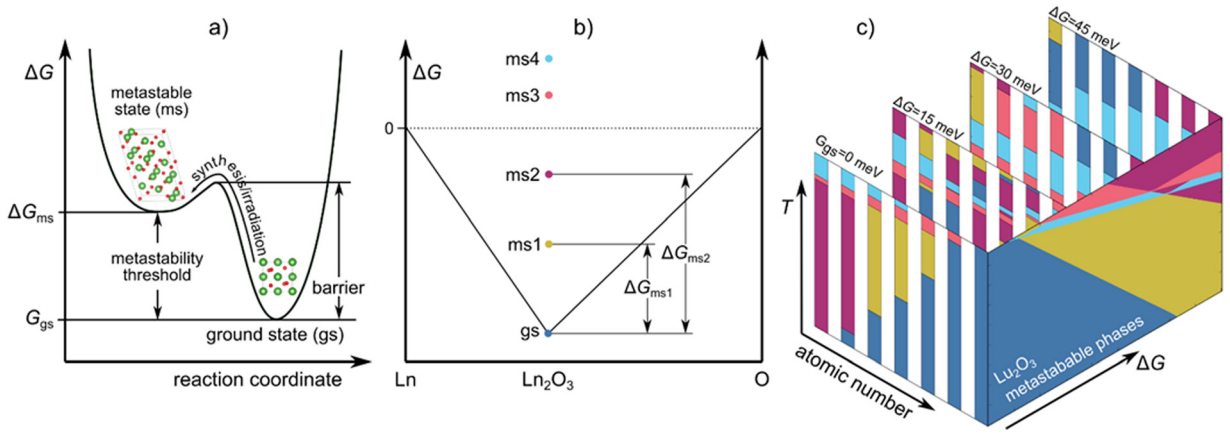

Fig. 1 (a) Schematic representation of a potential energy surface: the location of the local (metastable) and global (ground state) minima, the energy barrier to reach the metastable phase, and the metastability threshold. (b) Schematic representation of the Ln–O convex hull (black line), with a ground state phase and four metastable phases at Ln_2O_3 composition. ΔG_{ms1} ... ΔG_{ms4} are the energies above the convex hull of the ms1 ... ms4 phases, respectively, termed here as metastability threshold for those phases. (c) Schematic representation of calculated Ln_2O_3 phase diagrams at the ground state (ΔG = 0) and different values of ΔG, along with the corresponding metastable phases of Lu_2O_3, as function of ΔG and T. The five different colors represent the five different phases, which are described in the next figure.

experimental findings, provides a more fundamental understanding of observed phenomena, and predicts novel phases. However, there are limited number of DFT studies focused on the formation of metastable phases and the thermodynamic conditions for their formation.[20–25] This work goes beyond the previous studies by focusing on the stability and formability of metastable Ln_2O_3 polymorphs using various synthesis methods and irradiation, utilizing calculated thermodynamic properties of these structures.

For the purpose of our study, we chose Ln_2O_3 with Ln = La, Nd, Sm, Gd, Dy, Er, and Lu, lanthanides that display different phase behavior at low and high temperatures, as shown in Fig. 2a, while capturing chemical trends over the entire lanthanide series. This system provides a valuable case study for testing methodology as the phase behavior varies systematically with chemistry, and there is extensive experimental data of phase formation under non-equilibrium conditions to compare against. We compare the calculated and experimental phase stability of the different Ln_2O_3 phases as a function of chemistry. We then calculate the metastable phase diagrams, from which we extract the metastability threshold of the studied phases – defined to be the amount of stored energy at which that phase becomes competitive with the ground state phase – and correlate it with the experimentally observed metastable phases to rationalize and predict the formation of metastable phases. To test and validate our predictions, we synthesized Lu_2O_3 pellets, irradiated them to different fluences, and characterized the irradiated structures. Our results highlight how first-principles thermodynamics can be used to assess, interpret, and even predict the metastability of compounds under non-equilibrium conditions, providing new avenues for materials design. Also, our work demonstrates that multiple phase transitions are possible under increasing irradiation fluence, increasing our ability to tune the structure and thus the applicability of materials.

More rigorous approaches would consider the influence of defects on phase stability, the kinetic mechanisms that dictate the rate at which phases transform and the lifetime of metastable phases. However, the prohibitively high computational cost of accounting for all such effects makes such an approach feasible only for a very small set of structures and chemistries. The main goal of this study is to showcase that a simple computational approach can provide an initial, computationally inexpensive screening for the possibility of accessing metastable phases, based on the energy required for their formation.

Methodology

Calculations

DFT calculations were performed using the Vienna *Ab initio* Simulation Package (VASP).[26–29] The electron exchange correlation was modeled using the generalized gradient approximation (GGA) of Perdew, Burke and Ernzernhof parametrization for solids (PBEsol)[30] and projector augmented wave (PAW) potentials.[31,32] We chose PBEsol because it was the only functional amongst the five functionals we tested (the others are PBE,[33] revPBE,[34] PW91[35] and SCAN[36]) that correctly reproduced the stability of the A phase of La_2O_3. For the lanthanides (Ln) we used the PAW potentials from the VASP distribution with formal valence of 3, that is "Ln_3" and La pseudopotentials. We used these PAW potentials because the formal valency of 3 agrees with the valence state (+3) of the cations in the studied Ln_2O_3 oxides. The unit cells of the different phases were fully relaxed using a cut-off energy of 520 eV for expanding the electronic wave functions. Convergence criteria of 0.001 eV $Å^{-1}$ and 10^{-6} eV were adopted for the forces and total energy, respectively, and a γ-centered k-point spacing of <0.025 $Å^{-1}$ was applied for sampling the Brillouin zone for each structure.

To model the partial occupancy of the O site in the disordered phases, H and X, we generated special quasirandom

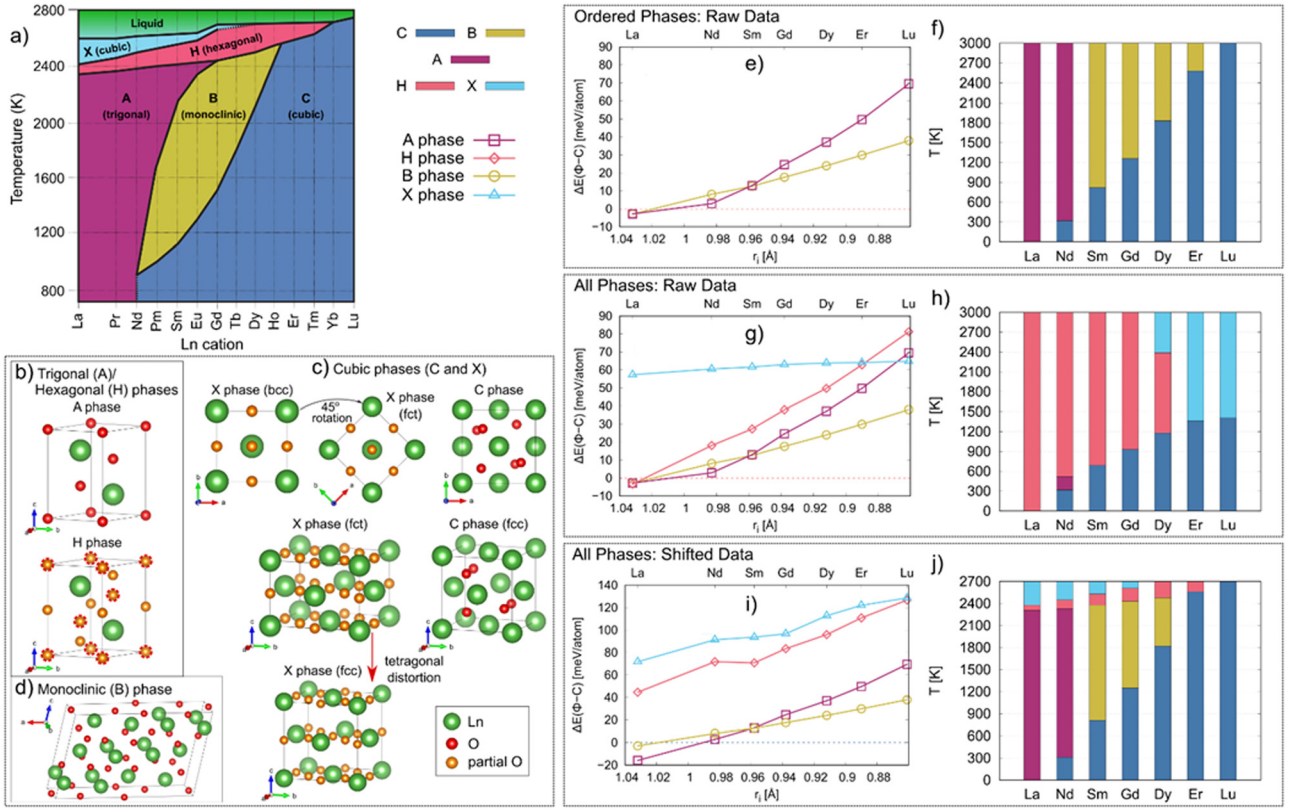

Fig. 2 (a) Phase diagram of the Ln_2O_3 (Ln = La–Lu) oxides [Adapted from ref. 39]. The C, A, H, B and X phase regions are shown in blue, magenta, red, yellow, and light blue, respectively. Structures of Ln_2O_3 phases: (b) trigonal/hexagonal (A and H), (c) cubic (C and X), and (d) monoclinic (B) phases. The Ln and O atoms are shown in green and red, respectively. The partially occupied O sites are shown in orange. For better comparison between the A and H phases, in the H phase structure the O sites also occupied in the A phase are circled with red dashed lines. Evidently, the H phase contains the same O sites as the A phase; hence, the H phase can be viewed as an oxygen disordered variant of the A phase. The cationic sublattice of the X phase is body center cubic (bcc) which can be turned into body center tetragonal (bct) by a 45° rotation around the *c*-axis (c). The arrow highlights how a tetragonal distortion along the *c*-axis would make the X phase cationic sublattice shift from bct to fcc, the same as the cationic sublattice of the C phase (c). (e) Energy of the ordered phases Φ relative to the C phase, $\Delta E(\Phi-C)$, as a function of the cationic radius (r_i), as calculated *via* DFT. (f) Phase stability regions in Ln_2O_3 as a function of temperature. (g) Energy of all studied phase (ordered and disordered) relative to the C phase, $\Delta E(\Phi-C)$, as a function of the cationic radius (r_i) as calculated by DFT. (h) Phase stability regions in Ln_2O_3 as a function of temperature. (i) Adjusted $\Delta E(\Phi-C)$ for all studied phases (see text for details). (j) Phase stability regions as a function of temperature based on adjusted energies. The data for the C, A, H, B and X phases are shown in blue (dashed line), magenta (squares), red (diamonds), yellow (circles), and light blue (triangles), respectively.

structures (SQS) of their 2 × 2 × 2 supercell of the conventional cells having $\frac{1}{2}$ oxygen using the *mcsqs* tool.[37] Note that the H phase structure of La_2O_3 reported in ICSD has two different O sites (2a and 4f), and when generating the SQS we considered that both sites are independently occupied. Also, the H phase structure in ICSD has partially occupied cationic sites, but the two sites are spatially very close to each other, separated by only 0.28 Å, and thus, we considered the cations to occupy only one site having average coordinates of the two sites. The relaxed crystallographic parameters of the studied polymorphs for all studied chemistries are given in Table S1 (ESI†).

To evaluate the stability of the different phases at finite temperature, the vibrational contribution to the free energy is required, which can be calculated using the phonon dispersion. The phonon dispersion, in turn, was calculated using the PHONOPY code,[38] employing the finite displacement method in a 2 × 2 × 2 supercell of each phase's respective unit cell, except for the A and B phases, for which we used different supercells to obtain positive phonon frequencies (see Fig. S1a and b, ESI†). For the A phase we used a 3 × 3 × 2 supercell, while for the B phase we used a 1 × 4 × 2 supercell. Note that we chose these supercell sizes because the three lattice parameters are much closer to each other compared to a 2 × 2 × 2 supercell. For the B phase we also had to explicitly specify the B phase primitive cell vectors (0.5, 0.5, 0.0) (−0.5, 0.5, 0.0) (0.0, 0.0, 1.0) to obtain positive phonon frequencies (see Fig. S1b, ESI†). The X phase exhibits imaginary phonon frequencies (see Fig. S1c, ESI†), which means that the relaxed structure is dynamically unstable, and a more stable structure with slightly different phonon dispersion exists (possibly related to relaxation of the oxygen associated with short-ranged order). However, the imaginary phonon band is very small, and therefore, removing this band would have a minimal influence on the vibrational entropy of the X phase.

The vibrational contribution to the free energy, F_{vib}, was calculated using the equation:

$$F_{vib} = \int_0^{\omega_{max}} \frac{\hbar\omega}{2} g(\omega) d\omega + Tk_b \int_0^{\omega_{max}} \ln\left[1 - \exp\left(-\frac{\hbar\omega}{k_b T}\right)\right] g(\omega) d\omega, \quad (1)$$

where T is the temperature, k_b is Boltzmann constant, $\hbar$ is the reduced Planck constant, $g(\omega)$ is the phonon density of states, and the integral is over all phonon frequencies, ω, up to the cut-off, ω_{max}. F_{vib} was subsequently used to evaluate the standard Gibbs energy, $G(T)$, using:

$$G(T) = E + F_{vib}, \quad (2)$$

where E is the DFT calculated total energy of the relaxed structure. Note that we did not consider the electronic and magnetic entropy because Ln_2O_3 are insulators, hence the electronic entropy is negligible, and our calculations show that they are non-magnetic. In the case of the disordered phases, the configurational entropy, S_{conf}, influences $G(T)$, and thus it should be added to eqn (2), obtaining:

$$G(T) = H + F_{vib} - TS_{conf}. \quad (3)$$

S_{conf} is calculated using Boltzmann's entropy formula:

$$S_{conf} = k_B \ln\left(\prod_i W_i\right), \quad W_i = \frac{g_i!}{n_i!(g_i - n_i)!}, \quad (4)$$

where W_i is the number of possible configurations of site i, and the product is over all partially occupied sites. g_i is the degeneracy of the partially occupied site i, and n_i is the number of atoms in partially occupied site i. Note that although the oxygen sites in both H and X phases are half filled, their $\prod_i W_i$ are different. The H phase has two partially occupied oxygen sites with g = 2 and 4, while the X phase has only one partially occupied oxygen site with g = 6. The different degeneracy of the O sites in the H and X phase gives rise to $\prod_i W_i$ of 12 and 20, respectively. The use of SQS and eqn (4) to describe these disordered compounds inherently assumes that they are randomly disorder. Recent work has shown that these types of materials exhibit short range order in their disordered state.[40] However, we have shown that the fully random limit reproduces experimental trends in disordering tendencies[41] and so, for convenience, we make that assumption here.

The metastable phase diagrams were built using the approach described by Srinivasan *et al.*[25] First, the metastable Gibbs energy, $\Delta G_{ms}(T)$, is calculated as:

$$\Delta G_{ms}(T) = G_{ms}(T) - G_{gs}(T), \quad (5)$$

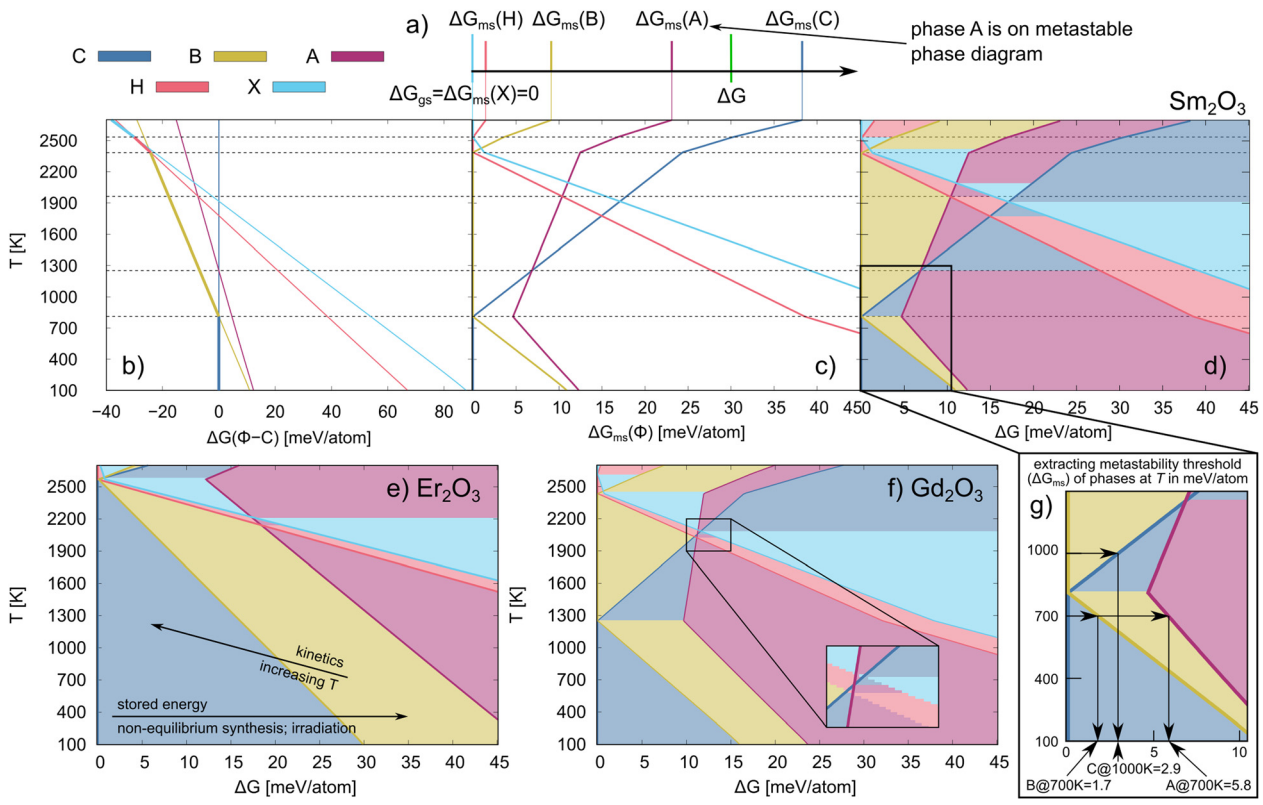

Fig. 3 (a) Schematic representation of the approach for identifying metastable phases (see eqn (6)). (b) $G(T)$ of Sm_2O_3 phases relative the C phase, ΔG (Φ−C) as function of temperature; the thicker lines represent the ground state phases. (c) Metastability threshold of the Sm_2O_3 phases as a function of temperature, *i.e.*, the free energy of the different polymorphs relative to the ground state phase at temperature T. (d) Sm_2O_3 metastable phase diagram. The dashed lines connect temperatures at which the ground state changes or there is a change in the metastable phase. Metastable phase diagrams for (e) Er_2O_3 and (f) Gd_2O_3. In (e), the lines indicate how different drivers push the system in different directions along the metastable phase diagram. The inset in (f) shows one example where multiple metastable phases intersect. (g) Schematic representation of the method for extracting the metastability threshold (ΔG_{ms}) of different phases at given T from a metastability phase diagram. The C, A, H, B and X phases are shown in blue, magenta, red, yellow and light blue, respectively.

where $G_{gs}(T)$ and $G_{ms}(T)$ are the Gibbs energy of the ground state (gs) phase, *i.e.*, the convex hull, and the metastable (ms) phase, respectively, at temperature T. $\Delta G_{ms}(T)$ represents the energy of the metastable phase above the convex hull at specific T, which is schematically shown in Fig. 1a and b. Next, a Gibbs energy difference is defined, ΔG, such that, for a given ΔG, phase Φ will be represented if:

$$0 \leq \Delta G^{\Phi}_{ms}(T) \leq \Delta G, \quad \text{and} \leq \Delta G^{\Phi}_{ms}(T) > \Delta G^{\text{other phase}}_{ms}(T). \tag{6}$$

From eqn (5) is evident that varying ΔG gives us the energy of the metastable phases with respect to the ground state (energy above the convex hull) at specific T (see Fig. 1b). The resulting ΔG_{ms} can be considered as the energy that needs to be added to a system to reach a given metastable phase, termed metastability threshold.

From eqn (5) and (6), it is evident that for those Ln_2O_3 with multiple stable phases, the ground state phase will change with increasing temperature. Fig. 3b shows the free energy of the different phases relative to phase C while Fig. 3c shows the free energy of those phases relative to the ground state at temperature T for Sm_2O_3. Since the C phase is not always the ground state, the relative energies in Fig. 3b can be negative. However, by construction, they are always positive in Fig. 3c. Finally, in Fig. 3d, we present the metastable phase diagram of Sm_2O_3, in which the stability windows of the different polymorphs of Sm_2O_3 are shown *versus* temperature and ΔG – the metastable phase diagrams for all studied Ln_2O_3 chemistries are reported in Fig. S2 (ESI†). To find what energy is stored in an experimentally observed metastable phase Φ at temperature T, we extract the metastability threshold (ΔG_{ms}) from the metastable phase diagrams (see Fig. 1b). See Fig. 3g for more details how the metastability threshold is calculated. Note that the choice for the highest ΔG of 45 meV per atom for representing the metastable phase diagrams is arbitrary, and a better choice for the highest ΔG would be the thermodynamic limit – the energy difference between an amorphous phase and the ground state;[22] however, we do not know the thermodynamic limit for these compounds.

The metastable phase diagrams depend on $G(T)$, and hence, having reliable $G(T)$ is very important. From Fig. 2h it is evident that, using $G(T)$ solely based on our DFT calculations, the disordered phases dominate over the ordered phases, which arises from the added configurational entropy of the disordered phases, lowering their $G(T)$. Thus, to obtain better agreement with experiment, we resorted to an additive positive shift to the energies of the disordered phases, so their experimental phase transition temperatures are reproduced. To reproduce the linear trend in $\Delta E(\Phi\text{–C})$ as function of the cation type seen in Fig. 2g, we also added a negative shift to the energy of the La_2O_3 A phase. The shifting parameters applied to the enthalpies of each phase are given in Table S2 (ESI†) while the $\Delta E(\Phi\text{–C})$ resulting from applying those shifts are shown in Fig. 2i. Alternatively, DFT+U can be used, which has been shown to give better agreement with experimental order–disorder transition temperatures of lanthanide-containing pyrochlores;[42] however, we would need to find appropriate values of U for each chemistry and polymorph of Ln_2O_3 studied here because of the different coordination number of the cations in the different phases. That would be a challenging task, raising questions of how to compare energies of systems with different values of U, and in the end, reducing to another set of fitting parameters. We therefore choose the more pragmatic route here.

Experiments

Sample fabrication. Powders of 99.999% purity Lu_2O_3 sourced from Advanced Material Resources INC. were pressed at 400 MPa into 13 mm diameter pellets. The pressed pellets were sintered at 1650 °C for 7 days in an air atmosphere furnace. The resulting pellets were sectioned into two pieces and the inside region of the pellets were polished to a 1 μm finish using Al_2O_3 films followed by a final polishing with a colloidal silica polishing suspension. Lastly, the samples were kept at 50 °C until the ion irradiations were performed. The polished surfaces of the Lu_2O_3 wafers were characterized by Grazing Incidence X-ray Diffraction (GIXRD) which revealed the material was a phase-pure cubic material belonging to the $Ia\bar{3}$ space group (C phase) as in the mineral bixbyite.

XRD specifics. GIXRD measurements were performed on a Bruker AXS D8 Advance equipped with a Cu K-α source and a Goebel mirror to achieve a parallel beam condition to illuminate the surface of the sample at a grazing incidence angle of 1°. The angle selected for GIXRD measurements is above the critical angle of the material (0.39°) and probes an estimated 128 nm capturing diffraction information from past the peak damage region in the material while minimizing signal from the bulk. For collecting the diffracted beam from the sample, a LYNXEYE XE-T PSD detector operating in 0-D mode was used. The peaks in the GIXRD patterns were assigned to specific phases using simulated XRD patterns calculated using the cif files for the A, H, and X phases of La_2O_3, and C and B phases of Sm_2O_3, taken from the Inorganic Crystal Structure Database (ICSD). Initially, the DFT calculated lattice parameters for the 5 different phases of Lu_2O_3 were used in the cif files, which were subsequently scaled to match the measured GIXRD peaks.

Ion irradiations. Ion irradiations of the prepared Lu_2O_3 materials were irradiated at the Ion Beam Materials Laboratory at Los Alamos National Laboratory, using a 200 kV Danfysik High Current Research Ion Implanter using 300 keV Kr^{++} ions. The samples were bonded to a cryogenic stage with silver paint to ensure good thermal contact while irradiated at 77 K under vacuum at four different fluences: 1×10^{19}, 8×10^{19}, 1×10^{20}, and 5×10^{20} Kr m^{-2} and a flux of 4×10^{16} Kr m^{-2} s^{-1}.

SRIM calculations. The conversion from irradiation fluence to dose (dpa) was done by performing Monte Carlo calculations using the program SRIM (Stopping and Range of Ions in Matter),[43] using a density of 9.42 g cm^{-3} and displacement threshold energies (E_d) of 40 eV for Lu and O.

Scanning/transmission electron microscopy. Scanning/transmission electron microscopy (S/TEM) foils were prepared using a FIB lift-out technique. The foils were attached and thinned on a Cu TEM half grid. Final thinning was done at

2 keV to eliminate the Ga beam damage before examination in the STEM. An FEI/Thermo Fisher Titan G2 80-300 S/TEM with a monochromator and an image aberration corrector was used to characterize film internal microstructure. Conventional TEM and selected-area electron diffraction (SAED) patterns were obtained using a C2 aperture of 150 μm and a selected area aperture of 10 μm.

Results

Before detailing the connection between experiments and calculations of metastable phases, we examine the energetics of the ordered and disordered phases, and how well the experimental phase transition temperatures are reproduced by DFT. We then discuss the relation between experimentally observed phases and their metastability threshold. Lastly, we focus on Lu_2O_3, a perfect model system for the examination of metastable phase formation, the relationship between predicted metastable phases, and the formation of these phases under irradiation.

Ordered phases

Of the five phases reported in the experimental phase diagram in Fig. 2a, three – A, B, and C – are ordered, in the sense that each Wykoff position in the crystal structure has an occupancy of one. Of these ordered phases, we found that the C phase is the most stable phase at 0 K for each of the studied Ln_2O_3 oxides, except for La_2O_3 for which the A phase is the most stable. Thus, we used the energy of the C phase as a reference to compare the stability of other phases Φ, with Φ = A or B: $\Delta E(\Phi\text{–C}) = E_\Phi - E_C$. This energy is shown in Fig. 2e. Clearly, $\Delta E(\Phi\text{–C})$ monotonically decreases with increasing cationic radius, from Lu to La, until eventually the A and B phases become more stable than C for La_2O_3. The energy difference between the A and B phase also increases with increasing cationic radius, with the A phase being more stable than the B phase for La_2O_3 and Nd_2O_3, while the two phases are nearly degenerate in energy for Sm_2O_3. This agrees with the experimental observation that both La_2O_3 and Nd_2O_3 form the A phase at lower temperatures (Fig. 2a). Also, the lower energy of the B phase compared to the A phase for those cations smaller than Sm reinforces the notion that the A phase structure for these cations is the transition state towards the B phase.[44]

The finite temperature stability of the phases shown in Fig. 2f, obtained by calculating their Gibbs energies $G(T)$ (eqn (2)) as detailed in the Methods, are directly comparable with experiments. We correctly find that La_2O_3 should only form the A phase, while the B phase energy is negligibly higher (ΔE(B–A) < 0.1 meV per atom), suggesting that, in principle, both phases should be able to form. However, the B phase of La_2O_3 is dynamically unstable, which explains why the B phase has not been reported for La_2O_3. In the case of Nd_2O_3, we find that the A phase should form above 320 K, which is close to room temperature (298.15 K) where the A phase has been reported experimentally. Interestingly, initial attempts at the synthesis of Nd_2O_3 reported the C phase at room temperature,[39,45,46] suggesting that the C phase might be stable at lower temperatures, but there are no measurements of a phase transition below room temperature or estimates of C → A transition temperature using thermodynamic modeling. When it comes to the other sesquioxides, we underestimate the C → B transition temperatures of Sm_2O_3, Gd_2O_3, and Dy_2O_3 by approximately 300 K. On the other hand, we reproduce the experimental C → B phase transition temperature for Er_2O_3, while Lu_2O_3 is stable in the C phase up to the melt, ∼2800 K. Overall, while there are some quantitative differences between our predictions and the experimental literature, the trends in the phase stability of the ordered phases *versus* chemistry are well reproduced by our calculations.

Disordered phases

We now turn to the relative stability of the disordered phases, H and X-the phases with partially occupied O sites. Fig. 2g compares their stability relative to the C phase and the other ordered phases. Both the H and X phases have higher energies compared to the other three phases, except for La_2O_3, for which the energies of the A and H phase are degenerate, and for Lu_2O_3, for which the X phase has lower energy than both the A and H phases. There is an apparent relationship in the energy differences between the X and C phase, and the A and H phase, with these two energy differences being almost constant along the Ln series. This trend is a reflection of the structural relation between these phases, as shown in Fig. 2b and d. Further, the close structural relationship between the A and H phase gives rise to similar phonon dispersions, with some matching bands (note the purple bands in Fig. S1d, ESI†).

To evaluate the phase stability regions *versus* temperature of the disordered phases, we calculate their $G(T)$, shown in Fig. 2h, using eqn (3). Clearly, and in contrast to experiment, the disordered phases H and X dominate the phase stability region of for all Ln_2O_3, and are the only phases present in addition to the C phase. The only exception is Nd_2O_3, where a small stability region for the A phase is identified; however, this stability region is smaller by an order of magnitude compared to experiment. In contrast, and as discussed above, we were able to reproduce the phase stability of the ordered phases. Thus, to obtain better agreement with experiment, we resort to empirically correcting our DFT energies by adding a positive shift to the energies of the disordered phases, as shown in Fig. 2i, so the experimental phase transition temperatures are reproduced (see Fig. 2j); see Methods section for more details. This amounts to an added enthalpic penalty for the disordered phases. Alternatively, the configurational entropy could be modified to include contributions from short-range ordering, known to reduce the magnitude of configuration entropy in disordered phases;[47] however, identifying the detailed short-range order of a disordered compound as a function of temperature requires extensive experiments and/or calculations, both of which are outside of the scope of this study. Thus, while multiple factors may account for the discrepancy between the theoretical and experimental $G(T)$ for these disordered phases,

we choose to incorporate that difference as a shift in the enthalpy.

Metastable phase diagram

We use the methodology of Srinivasan *et al.*[25] to construct metastable phase diagrams of the Ln_2O_3 compounds. In this methodology, a Gibbs energy difference (ΔG) determines which phase is considered as metastable (see Methods section); the concept is schematically illustrated in Fig. 3a, and the physics of ΔG is detailed in Methods section. ΔG is a variable that represents the amount of excess energy in the system – the amount of energy above the ground state for which we will determine which metastable phase is present; we refer to the lowest energy at which a given metastable phase is present as the metastability threshold for that phase. Note that this threshold depends on temperature and chemistry. The method for extracting the metastability threshold at synthesis temperature from metastable phase diagrams is schematically represented in Fig. 3g. The metastability threshold can also be viewed as the stored energy that is needed for the metastable phase to be produced. The stored energy can be introduced using different synthesis methods, such as decomposition of salts or other non-equilibrium synthesis (sputtering, filtered cathodic arc, molecular beam epitaxy), or by irradiation.

Detailed in Table 1 are experimentally synthesized Ln_2O_3 metastable phases that have been reported in the literature, including their synthesis method, temperature, and metastability threshold (ΔG_{ms}) as determined by our analysis. This metastability threshold can be viewed as the amount of stored energy in the ground state at which the indicated phase becomes energetically competitive. That is, conceptually, if we introduce an excess energy of ΔG_{ms} into the ground state phase, the associated metastable phase will be degenerate in energy (assuming it has no stored energy of its own). *Via* synthesis from salts and hydrothermal synthesis, only those Ln_2O_3 oxides with cationic radii larger than Gd are reported to form metastable phases. The reason for the anomalous behavior of La_2O_3 is the high stability of the A phase, which yields a large metastability threshold (>19 eV per atom at 300 K) for the other phases (see Fig. S2a, ESI†), requiring different methodology, such as molecular beam epitaxy with stabilization *via* strain, to produce the metastable C phase. Layers of metastable C phase of Nd_2O_3 and B phase of Gd_2O_3 have also been produced by magnetron sputtering and molecular beam epitaxy. In the case of the smaller cations, introducing a sputtering power[56] or negative biased voltage[55] helps in producing the B phase of Er_2O_3, although its metastability threshold is large (see Table 1 and Fig. 1a).

Another way to produce metastable phases with high metastability thresholds at low temperatures is by irradiation. Tang *et al.* have shown that irradiating the C phase of Dy_2O_3 and Er_2O_3 with 300 keV Kr^{++} ions at 120 K produces the B phase[57] and the H phase for Dy_2O_3,[58] with the lowest irradiation dose producing the B and H phases listed in Table 1. The higher irradiation dose required for Er_2O_3 agrees with the larger metastability threshold of Er_2O_3 compared to Dy_2O_3 (see Table 1). Also, the higher irradiation dose used to produce Dy_2O_3 H phase correlates with the larger metastability threshold of the H phase than the B phase.

Irradiation of Lu_2O_3

To validate the computational results presented above, we consider the formation of metastable phases *via* stored energy

Table 1 List of oxides for which metastable phases have been reported to be synthesized/formed from the literature, including the synthesis method and synthesis temperature at which the metastable phase was achieved. The metastable phase type is noted as Φ. The last three rows show metastable phases produced by irradiation, including the irradiation method and dose, in displacements per atom (dpa), that gives an apparent yield of 10% of the metastable phase. The last column reports our calculated metastability threshold (ΔG_{ms}), see Fig. 2g, of the experimentally produced metastable phases at the synthesis/irradiation temperature

Oxide	Φ	Synthesis method/radiation	T [K]	Ref.	ΔG_{ms}
Nd_2O_3	C	Hydrothermal	970	48	6.9
Nd_2O_3	B	Hydrothermal	1205	48	3.1
Nd_2O_3	C	Nitrate solid state	860, 1080	45 and 49	6.5, 8.0
Nd_2O_3	C	Carbonate decomposition	790, 820–1020	45 and 49	5.3–7.4
Nd_2O_3	C	Oxalate decomposition	820, 920–1020	45 and 49	6.4–7.4
Nd_2O_3	C	Hydroxide decomposition	820–1020	45	5.3–7.4
Nd_2O_3	C	Acetate combustion	1050	45	7.7
Sm_2O_3	B	Fused nitride decomposition	700	50	1.8
Sm_2O_3	C	Chloride decomposition	1170	51	5.6
Gd_2O_3	B	Fused nitride decomposition	700	50	7.8
La_2O_3	C	Molecular beam epitaxy <2 nm	1020	52	27.2
Nd_2O_3	C	Molecular beam epitaxy	950	53	6.6
Nd_2O_3	C	Magnetron sputtering	420	18	1.2
Gd_2O_3	B	Magnetron sputtering system	920	54	4.6
Gd_2O_3	B	Molecular beam epitaxy	520	19	10.2
Er_2O_3	B	Pulsed magnetron sputtering	<620	55	23.8
Er_2O_3	B	Filtered cathode Arc	<770	56	21.9
Dy_2O_3	B	300 keV Kr^{++} ions; 5 dpa	120	57	22.3
Er_2O_3	B	300 keV Kr^{++} ions; 17 dpa	120	57	29.8
Dy_2O_3	H	300 keV Kr^{++} ions; 125 dpa	120	58	91.1

introduced by irradiation. Of the studied Ln_2O_3, Lu_2O_3 is an excellent compound for further study because of its easy synthesizability to high purity and the high stability of the C phase. Also, our calculations show significant differences between the metastability threshold of the Lu_2O_3 metastable phases (see Fig. 4c), allowing for distinct separation of metastable phase formation with increasing stored energy, such as that introduced by increasing irradiation fluence. We irradiated Lu_2O_3 to four different fluences (see Methods section), covering a wide range of stored energy to access multiple metastable phases. As revealed in Fig. 4a, grazing incidence X-ray diffraction analysis of the irradiated Lu_2O_3 pellets shows that, at the lowest fluence of 1×10^{19} Kr m^{-2}, only the B phase is formed. At 8×10^{19} and 1×10^{20} Kr m^{-2}, a mixture of the A and X phases is observed. Increasing the fluence to 5×10^{20} Kr m^{-2} produces primarily the X phase. While it has been shown that *e.g.* MAX phases can also undergo multiple phase transitions under increasing irradiation fluence,[59–61] reports of multiple phase transformations under increasing fluence are rare.

For additional characterization of the irradiated Lu_2O_3 pellets we used scanning/transmission electron microscopy (S/TEM) (Fig. 4d) and selected area electron diffraction (SAED)

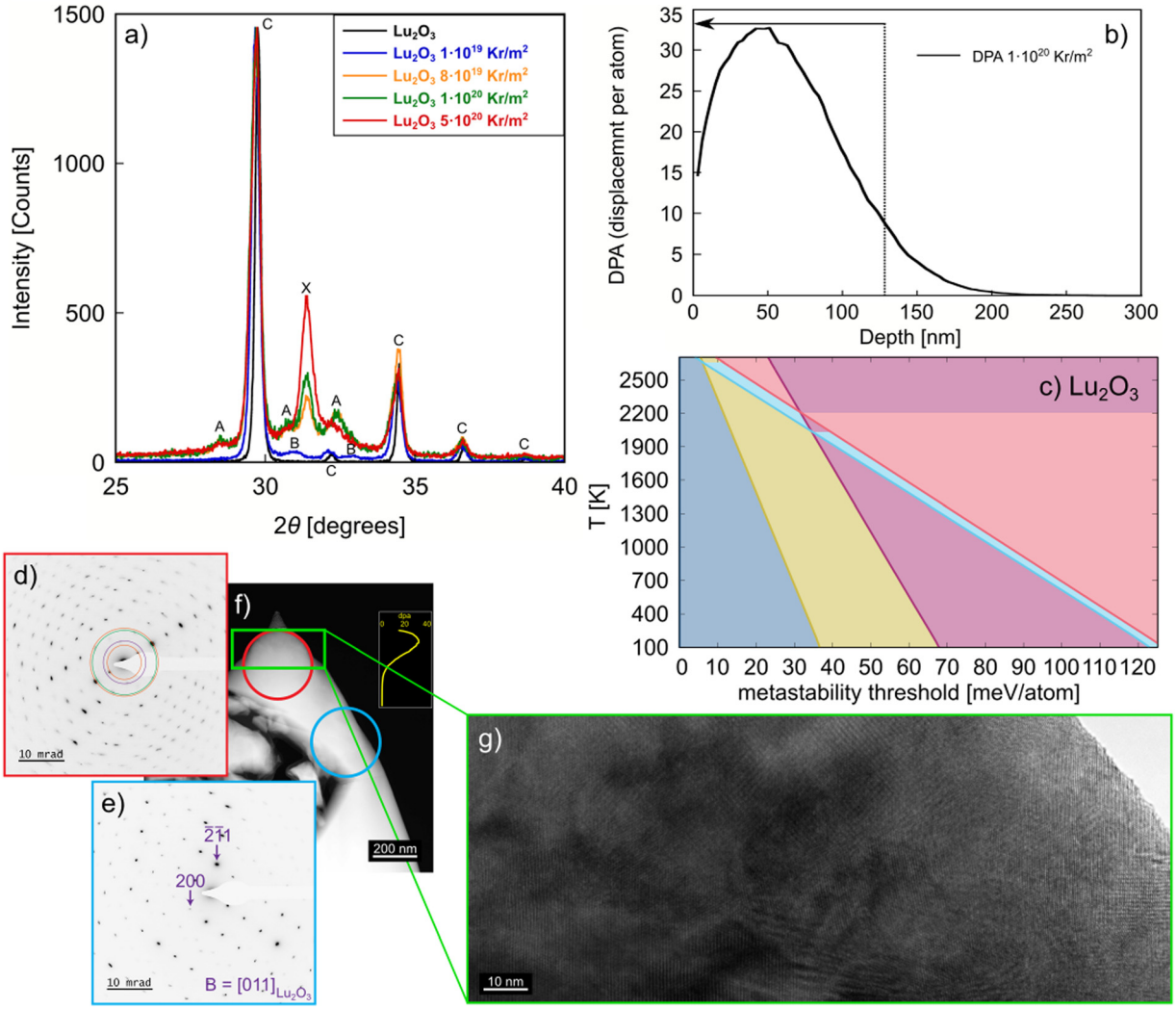

Fig. 4 (a) GIXRD (Grazing Incidence X-ray Diffraction) patterns obtained from pristine Lu_2O_3 and ion irradiated Lu_2O_3 over a fluence range of 1×10^{19} to 5×10^{20} Kr m^{-2} with 300 keV Kr^{++} ions at 120 K. Pristine Lu_2O_3 and samples irradiated to 1×10^{19}, 8×10^{19}, 1×10^{20}, and 5×10^{20} Kr cm^{-2} are shown in black, blue, orange, green, and red, respectively. The GIXRD measurements probe an estimated 128 nm in depth, primarily sampling the irradiated region and minimizing the signal from the unirradiated substrate. The GIXRD measurements show the phase progression from C → B → A + X → X phases as a function of fluence. (b) SRIM (Stopping and Range of Ions in Matter) simulation results showing the displacement damage profile as function of depth for 1×10^{20} Kr m^{-2} 300 keV Kr^{++} ions into Lu_2O_3. The dashed line and arrow indicate the estimated depth probed by the 1° X-ray incidence angle for the measurements shown in (a). (c) Metastable phase diagram of Lu_2O_3. (d) A Z-contrast image of the irradiated portion of the sample; the yellow curve in the inset is the SRIM profile (as shown also in b), depicting the penetration depth of the irradiation beam. (e) Selected area electron diffraction pattern (SADP) of the polycrystalline, irradiated portion of the sample irradiated at 1×10^{20} Kr m^{-2} as demarcated by the red encircled region. (f) A SADP from the blue encircled region of the unirradiated portion of the Lu_2O_3 sample showing a cubic [011] zone axis. The polycrystalline microstructure of the irradiated portion is doubly confirmed by the high-resolution image in (g), which shows nanograins of differing orientation.

of the irradiated region (Fig. 4e) and the bulk of the pellet (Fig. 4f). The irradiation depth in the Lu_2O_3 pellet is ~150 nm, as shown in Fig. 4b. A high-resolution S/TEM image of the irradiated region of the pellet is shown in Fig. 4g. Together, the S/TEM and SAED reveal the existence of multiple phases in the irradiated region of Lu_2O_3, and the C phase in the unirradiated region of the pellet, indicating that the radiation-induced phase transformation involves a complex post-irradiation microstructure. We note that these results are in contrast with previous experiments, which reported no phase transition in irradiated Lu_2O_3.[57] This sequence of metastable phases – C → B → A + X → X – is very close to the sequence of metastable phases we predict for this system, as highlighted in Fig. 4c.

Discussion

As schematically illustrated in Fig. 1a, a metastable phase occupies a local minimum on the potential energy surface (PES), separated by a barrier from the deepest (global) minimum, *i.e.*, the ground state. This energy barrier between the two minima needs to be overcome to produce the metastable phase, which can be achieved through synthesis, irradiation, or change in pressure. In the case of the metastable phases produced by thermal synthesis there is an apparent limit in the amount of stored energy achievable *via* these routes, about 8 meV per atom, and only Ln_2O_3 with Ln = Nd–Gd are within this limit, as shown in Table 1. The Ln_2O_3 with smaller ions, on the other hand, have metastability thresholds above this limit (>10 meV per atom; see Fig. S2, ESI†), which explains why only their ground state (the C phase) has been synthesized. It is also worth noting that using different salts at the same synthesis temperature can produce different phases,[62] and that synthesizability depends on the oxygen partial pressure.[54] Not surprisingly, this indicates that the synthesizability of a metastable phase is also dependent on the synthesis pathway, in addition to the metastability threshold, and that knowing the metastability threshold is only part of the story.

As illustrated in Fig. 3e, increasing the temperature lowers the metastability threshold, allowing, in principle, for easier production of the metastable phases – less stored energy is needed to access the metastable phases. However, at elevated temperatures the rate of kinetic pathways is also increased, providing easier access to the equilibrium phases – as described in Fig. 1a, the rate of overcoming the barrier from the metastable phase to the ground state is higher at higher temperature. In the case of Nd_2O_3, both Stecura[49] and Glushkova *et al.*[45] show that the dominant phase at higher temperatures is the ground state A phase regardless of the Nd salt used, while Wendlandt showed that Sm and Gd also form their ground state phases at elevated temperatures.[51] This indicates that, although the metastability threshold is decreased at higher temperatures, the kinetic hindrance is also removed, and the system can reach the thermodynamically-preferred the ground state phase. Hence, increasing the temperature is not enough to overcome the metastability threshold of those oxides with a higher threshold (Ln_2O_3 oxides with smaller ions and La_2O_3), and other non-equilibrium methods need to be applied. The negative biased voltage and sputtering power used in some synthesis approaches add enough energy at lower temperature to overcome the metastability threshold of Er_2O_3 without influencing the kinetics. As in the case of the other Ln_2O_3 oxides, increasing the temperature stabilizes the ground state C phase of Er_2O_3 in both synthesis methods. Metastable phase formation can be promoted by growing the Ln_2O_3 on a substrate that supports the metastable phase formation *via* strain or isomorphic structure. This is the case of the metastable C phase of La_2O_3 which can be stabilized on Si(111) substrates for a thickness up to 2 nm, though increasing the thickness produces the ground state A phase.[52] It is also worth noticing that the metastable B phase has not been observed for neither La_2O_3 nor Lu_2O_3. In the case of La_2O_3, we determine that to be because of the dynamical instability of the La_2O_3 B phase. In contrast, for Lu_2O_3, there is a significant metastability threshold of the Lu_2O_3 B phase. To overcome this large metastability threshold, the temperature must be increased, but in this case the melt becomes thermodynamically favorable first. Another way to add energy to the system while maintaining a low temperature to prevent either kinetic recovery or a shift in the thermodynamically preferred state is by irradiation, which we show is a practical way of producing Lu_2O_3 metastable phases.

Our experiments confirm that irradiation can be used to produce multiple metastable phases that are not on the phase diagram of Lu_2O_3, essentially moving to the right in our calculated metastable phase diagram shown in Fig. 4c. The observed sequence of phases with increasing irradiation fluence agrees with the increasing metastability threshold of the B, A and X phases, as shown in Fig. 4c. It is also worth noting that the highly metastable X phase that is reported to form when swift heavy ion irradiation is used,[44] in which the system is essentially brought down from the melt, can also be produced by gradually introducing stored energy, as done here. Interestingly, the metastable phases resemble a sequence of ground state phases of larger cations than Lu at increased temperatures, basically moving diagonally in the Ln_2O_3 phase diagram shown in Fig. 2a.

Our observations align with Wigner's stipulation that, with increasing fluence, the defect concentration in a phase increases, and hence, the internal energy of that phase is also increased.[63] At the same time, the increased defect concentration will act to lower the nucleation barrier for the kinetics to drive a phase transition[64] which, with the increased internal energy, will cause the phase transition to a metastable phase. At this time we cannot identify which defects are responsible for the phase transformations.

As defined in ref. 25 and performed here, this methodology provides information about the energy difference between the global and local minima of phases on the PES. A more complete picture of the PES schematically illustrated in Fig. 1a contains information on the width of the minima (basin of attraction) and the lifetime of the metastable phases (the barriers between them). Further, we have, for the sake of pragmatism, made

several assumptions that limit the fidelity of our results. For example, the free energy of a given phase will not only be dictated by the properties of the perfect crystal, but also the equilibrium and non-equilibrium defect content present. In addition, we have not accounted for any kinetic factors that may govern the actual phase-to-phase transformations. Finally, recognizing that the assumption of a random solid solution overestimates the configurational entropy of these materials, we have elected to shift the enthalpy rather than the entropy as a correction to our free energies. In reality, these materials exhibit short-ranged order, meaning that not all configurations are equally likely. However, calculating the temperature and chemistry-dependent configuration entropy would be a daunting task for one chemistry[65] and its associated phases, much less the full set of chemistries considered here. That said, and as discussed earlier, the approach used here can explain the relative metastability of the ordered phases; the issue arises when both ordered and disordered phases are compared, for which a more careful treatment of the entropy is required. If we did not calibrate the energetics of the disordered phases against experiment, then we would not have been able to relate the metastability of the disordered phases with experiments without significantly more computational effort.

Thus, accounting for all of these factors[21,66] is a very challenging and computational expensive endeavor. We have shown that using a simpler and computationally much less demanding approach is valuable for initial screening in search of functional metastable phases producible by ether synthesis or irradiation. For example, materials that exhibit dynamic regimes and sit at the intersection or in the vicinity of multiple phases on the PES, such as regions of the metastable phase diagrams where various phases co-exist (see inset Fig. 3f), can be more efficient heterogeneous catalysts.[67–69] A low metastability threshold indicates a possibly easy phase transition induced by electrical pulse, helping in discovering new materials for phase change memory devices. This approach can also help discover materials that are more radiation tolerant by predicting what phases can form under extreme conditions.'

Conclusions

In summary, we explained the formation of metastable phases, either by synthesis or irradiation, in the Ln_2O_3 family of compounds using the metastability threshold extracted from metastable phase diagrams. Furthermore, we demonstrate that multiple metastable phases of Lu_2O_3 can be formed under irradiation, with the phase formation sequence being correlated with their metastability threshold. We also identify a metastability limit ($\sim$8 meV per atom) above which metastable phases cannot be synthesized from decomposition of salts or hydrothermal synthesis. This explains why metastable phases of Ln_2O_3 with smaller cations (Ln = Tb–Lu) have not been synthesized *via* these approaches, and why other non-equilibrium synthesis methods or irradiation are required to produce metastable phases of these Ln_2O_3. These results provide new insight into the metastability of an essential class of compounds, help explain experimental results regarding their synthesis and irradiation behavior, and most importantly guide future experimental studies of these materials.

Conflicts of interest

The authors declare that they have no competing interests.

Acknowledgements

This work, performed at Los Alamos National Laboratory, was supported by the U. S. Department of Energy, Office of Science, Basic Energy Sciences, Materials Sciences and Engineering Division. Los Alamos National Laboratory is operated by Triad National Security, LLC, for the National Nuclear Security Administration of U. S. Department of Energy (Contract No. 89233218CNA000001). This work was performed, in part, at the Center for Integrated Nanotechnologies, an Office of Science User Facility operated for the U. S. Department of Energy Office of Science. Computational support for this work was provided by LANL's high performance computing clusters. This research also used resources of the National Energy Research Scientific Computing Center (NERSC), a U. S. Department of Energy Office of Science User Facility located at Lawrence Berkeley National Laboratory, operated under Contract No. DE-AC02-05CH11231 using NERSC award BES-ERCAP-0016919.

References

1 Q. Wang, *et al.*, Applications and recent advances of rare earth in solid oxide fuel cells, *J. Rare Earths*, 2021, **40**, 1668, DOI: 10.1016/j.jre.2021.09.003.
2 K. E. Sickafus, *et al.*, Radiation induced amorphization resistance in A2O3–BO2 oxides, *Nucl. Instrum. Methods Phys. Res., Sect. B*, 2002, **191**, 549–558.
3 G.-Y. Adachi and N. Imanaka, The Binary Rare Earth Oxides, *Chem. Rev.*, 1998, **98**, 1479–1514.
4 H. J. Osten, J. P. Liu and H. J. Müssig, Band gap and band discontinuities at crystalline Pr2O3/Si(001) heterojunctions, *Appl. Phys. Lett.*, 2002, **80**, 297–299.
5 K. H. Goh, A. S. M. A. Haseeb and Y. H. Wong, Lanthanide rare earth oxide thin film as an alternative gate oxide, *Mater. Sci. Semicond. Process.*, 2017, **68**, 302–315.
6 U. Griebner, *et al.*, Passively mode-locked Yb:Lu2O3 laser, *Opt. Express*, 2004, **12**, 3125–3130.
7 C. J. Saraceno, *et al.*, SESAMs for high-power femtosecond modelocking: power scaling of an Yb:LuScO3 thin disk laser to 23 W and 235 fs, *Opt. Express*, 2011, **19**, 20288–20300.
8 L. Hao, *et al.*, Spectroscopy and laser performance of Nd:Lu2O3 crystal, *Opt. Express*, 2011, **19**, 17774–17779.
9 F. Druon, *et al.*, and Yb:Y2O3 crystals grown by an original flux method, *Opt. Lett.*, 2013, **38**, 4146–4149.
10 H. X. Dai, C. F. Ng and C. T. Au, Raman spectroscopic and EPR investigations of oxygen species on SrCl2-promoted

Ln2O3 (Ln = Sm and Nd) catalysts for ethane-selective oxidation to ethene, *Appl. Catal., A*, 2000, **202**, 1–15.
11 B. M. E. Russbueldt and W. F. Hoelderich, New rare earth oxide catalysts for the transesterification of triglycerides with methanol resulting in biodiesel and pure glycerol, *J. Catal.*, 2010, **271**, 290–304.
12 Z. Taherian, *et al.*, A comparative study of ZrO2, Y2O3 and Sm2O3 promoted Ni/SBA-15 catalysts for evaluation of CO2/methane reforming performance, *Int. J. Hydrogen Energy*, 2017, **42**, 16408–16420.
13 M. Majumder, *et al.*, Impact of rare-earth metal oxide (Eu2O3) on the electrochemical properties of a polypyrrole/CuO polymeric composite for supercapacitor applications, *RSC Adv.*, 2017, **7**, 20037–20048.
14 V. S. Saji, Review of rare-earth-based conversion coatings for magnesium and its alloys, *J. Mater. Res. Technol.*, 2019, **8**, 5012–5035.
15 L. Zhou, *et al.*, Size-tunable synthesis of lanthanide-doped Gd2O3 nanoparticles and their applications for optical and magnetic resonance imaging, *J. Mater. Chem.*, 2012, **22**, 966–974.
16 J. Yin, *et al.*, Hollow-structured upconverting sesquioxide targeted nanoprobes for magnetic resonance and fluorescence combined imaging, *RSC Adv.*, 2016, **6**, 72836–72844.
17 V. Muthulakshmi, M. Balaji and M. Sundrarajan, Biomedical applications of ionic liquid mediated samarium oxide nanoparticles by Andrographis paniculata leaves extract, *Mater. Chem. Phys.*, 2020, **242**, 122483.
18 M. Shao, *et al.*, Effect of deposition temperature on structure and properties of Nd2O3 thin films prepared by magnetron sputtering, *Vacuum*, 2019, **169**, 108936.
19 P. Gribisch and A. Fissel, Tuning of structural and dielectric properties of Gd2O3 grown on Si(001), *J. Appl. Phys.*, 2020, **128**, 055108.
20 W. Sun, *et al.*, The thermodynamic scale of inorganic crystalline metastability, *Sci. Adv.*, 2016, **2**, e1600225.
21 V. Stevanović, Sampling Polymorphs of Ionic Solids using Random Superlattices, *Phys. Rev. Lett.*, 2016, **116**, 075503.
22 M. Aykol, *et al.*, Thermodynamic limit for synthesis of metastable inorganic materials, *Sci. Adv.*, 2018, **4**, eaaq0148.
23 A. Anelli, *et al.*, Generalized convex hull construction for materials discovery, *Phys. Rev. Mater.*, 2018, **2**, 103804.
24 J.-H. Pöhls, M. Heyberger and A. Mar, Comparison of computational and experimental inorganic crystal structures, *J. Solid State Chem.*, 2020, **290**, 121557.
25 S. Srinivasan, R. Batra, D. Luo, T. Loeffler, S. Manna, H. Chan, L. Yang, W. Yang, J. Wen, P. Datancet and S. K. R. S. Sankaranarayanan, Machine learning the metastable phase diagram of covalently bonded carbon, *Nat. Commun.*, 2022, **13**, 3251.
26 G. Kresse and J. Hafner, Ab initio molecular dynamics for liquid metals, *Phys. Rev. B: Condens. Matter Mater. Phys.*, 1993, **47**, 558–561.
27 G. Kresse and J. Hafner, Ab initio molecular-dynamics simulation of the liquid-metal–amorphous-semiconductor transition in germanium, *Phys. Rev. B: Condens. Matter Mater. Phys.*, 1994, **49**, 14251–14269.
28 G. Kresse and J. Furthmüller, Efficiency of ab-initio total energy calculations for metals and semiconductors using a plane-wave basis set, *Comput. Mater. Sci.*, 1996, **6**, 15–50.
29 G. Kresse and J. Furthmüller, Efficient iterative schemes forab initiototal-energy calculations using a plane-wave basis set, *Phys. Rev. B: Condens. Matter Mater. Phys.*, 1996, **54**, 11169–11186.
30 G. I. Csonka, *et al.*, Assessing the performance of recent density functionals for bulk solids, *Phys. Rev. B: Condens. Matter Mater. Phys.*, 2009, **79**, 155107.
31 P. E. Blöchl, Projector augmented-wave method, *Phys. Rev. B: Condens. Matter Mater. Phys.*, 1994, **50**, 17953–17979.
32 G. Kresse and D. Joubert, From ultrasoft pseudopotentials to the projector augmented-wave method, *Phys. Rev. B: Condens. Matter Mater. Phys.*, 1999, **59**, 1758–1775.
33 J. P. Perdew, K. Burke and M. Ernzerhof, Generalized Gradient Approximation Made Simple, *Phys. Rev. Lett.*, 1996, **77**, 3865–3868.
34 Y. Zhang and W. Yang, Comment on ''Generalized Gradient Approximation Made Simple'', *Phys. Rev. Lett.*, 1998, **80**, 890.
35 J. P. Perdew, *et al.*, Atoms, molecules, solids, and surfaces: Applications of the generalized gradient approximation for exchange and correlation, *Phys. Rev. B: Condens. Matter Mater. Phys.*, 1992, **46**, 6671–6687.
36 J. Sun, A. Ruzsinszky and J. P. Perdew, Strongly Constrained and Appropriately Normed Semilocal Density Functional, *Phys. Rev. Lett.*, 2015, **115**, 036402.
37 A. van de Walle, *et al.*, Efficient stochastic generation of special quasirandom structures, *Calphad*, 2013, **42**, 13–18.
38 A. Togo and I. Tanaka, First principles phonon calculations in materials science, *Scr. Mater.*, 2015, **108**, 1–5.
39 M. Foex and J. Traverse, Investigations about crystalline transformation in rare earths sesquioxides at high temperatures, *Rev. Int. Hautes Temp. Refract.*, 1966, **3**, 429–453.
40 J. Shamblin, *et al.*, Probing disorder in isometric pyrochlore and related complex oxides, *Nat. Mater.*, 2016, **15**, 507–511.
41 G. Pilania, *et al.*, Using Machine Learning To Identify Factors That Govern Amorphization of Irradiated Pyrochlores, *Chem. Mater.*, 2017, **29**, 2574–2583.
42 P. M. Kowalski, Formation enthalpy of Ln2B2O7-type (B = Ti,Sn,Hf,Zr) compounds, *Scr. Mater.*, 2020, **189**, 7–10.
43 J. F. Ziegler, M. D. Ziegler and J. P. Biersack, SRIM – The stopping and range of ions in matter, *Nucl. Instrum. Methods Phys. Res., Sect. B*, 2010, **268**, 1818–1823.
44 C. L. Tracy, *et al.*, Phase transformations in Ln_2O_3 materials irradiated with swift heavy ions, *Phys. Rev. B: Condens. Matter Mater. Phys.*, 2015, **92**, 174101.
45 V. B. Glushkova and A. G. Boganov, Polymorphism of rare-earth sesquioxides, *Bull. Acad. Sci. USSR, Div. Chem. Sci.*, 1965, **14**, 1101–1107.
46 I. Warshaw and R. Roy, Polymorphism of the rare earth sesquioxides, *J. Phys. Chem.*, 1961, **65**, 2048–2051.
47 A. D. Pelton and Y.-B. Kang, Modeling short-range ordering in solutions, *Int. J. Mater. Res.*, 2007, **98**, 907–917.
48 M. W. Shafer and R. Roy, Rare-Earth Polymorphism and Phase Equilibria in Rare-Earth Oxide-Water Systems, *J. Am. Ceram. Soc.*, 1959, **42**, 563–570.

49 S. Stecura, *Crystallographic Modifications and Phase Transformation Rates of Five Rare-earth Sesquioxides: Lanthanum Oxide, Neodymium Oxide, Samarium Oxide, Europium Oxide, and Gadolinium Oxide*, US Department of the Interior, Bureau of Mines, 1965, resreport.
50 G. Brauer and A. Siegert, Beiträge zur Polymorphie der Sesquioxide der Seltenen Erden. II. Über die Abscheidung von Seltenerdoxiden aus Nitratschmelzen, *Z. Anorg. Allg. Chem.*, 1969, **371**, 263–273.
51 W. W. Wendlandt, The thermal decomposition of the heavier rare earth metal chloride hydrates, *J. Inorg. Nucl. Chem.*, 1959, **9**, 136–139.
52 A. Proessdorf, *et al.*, Epitaxial polymorphism of La2O3 on Si(111) studied by *in situ* x-ray diffraction, *Appl. Phys. Lett.*, 2014, **105**, 021601.
53 J. Wang, T. Liu and Z. Wang, Crystalline Nanoscale M2O3 (M = Gd, Nd) (M = Gd, Nd) Thin Films Grown by Molecular Beam Epitaxy on Si(111), *Mater. Trans.*, 2009, **50**, 2115–2117.
54 Y.-L. Li, *et al.*, Effect of the oxygen concentration on the properties of Gd_2O_3 thin films, *J. Cryst. Growth*, 2004, **265**, 548–552.
55 X. Li, *et al.*, Crystallization behavior and mechanical properties of erbium oxide coatings fabricated by pulsed magnetron sputtering, *Thin Solid Films*, 2012, **520**, 2316–2320.
56 C. Adelhelm, *et al.*, Influence of deposition temperature and bias voltage on the crystalline phase of Er2O3 thin films deposited by filtered cathodic arc, *J. Nucl. Mater.*, 2011, **417**, 798–801.
57 M. Tang, *et al.*, Ion-irradiation-induced phase transformation in rare earth sesquioxides (Dy2O3,Er2O3,Lu2O3), *J. Appl. Phys.*, 2006, **99**, 063514.
58 M. Tang, *et al.*, Heavy ion irradiation effects in the rare-earth sesquioxide Dy2O3, *Nucl. Instrum. Methods Phys. Res., Sect. B*, 2006, **250**, 142–147.
59 C. Wang, *et al.*, Role of the X and n factors in ion-irradiation induced phase transformations of $Mn_{+1}AX_n$ phases, *Acta Mater.*, 2018, **144**, 432–446.
60 C. Wang, *et al.*, Disorder in $Mn_{+1}AX_n$ phases at the atomic scale, *Nat. Commun.*, 2019, **10**, 622.
61 C. Wang, C. L. Tracy and R. C. Ewing, Radiation effects in $Mn_{+1}AX_n$ phases, *Appl. Phys. Rev.*, 2020, **7**, 041311.
62 L. Eyring, The Binary Lanthanide Oxides: Synthesis and Identification, in *Synthesis of Lanthanide and Actinide Compounds*, ed. G. Meyer and L. R. Morss, Dordrecht, Springer, Netherlands, 1991, pp. 187–224.
63 E. P. Wigner, Theoretical Physics in the Metallurgical Laboratory of Chicago, *J. Appl. Phys.*, 1946, **17** 857–863.
64 X. Zhang, *et al.*, Defect-characterized phase transition kinetics, *Appl. Phys. Rev.*, 2022, **9**, 041311.
65 A. van de Walle and G. Ceder, The effect of lattice vibrations on substitutional alloy thermodynamics, *Rev. Mod. Phys.*, 2002, **74**, 11–45.
66 D. Turnbull and J. C. Fisher, Rate of Nucleation in Condensed Systems, *J. Chem. Phys.*, 1949, **17**, 71–73.
67 K. Reuter, D. Frenkel and M. Scheffler, The Steady State of Heterogeneous Catalysis, Studied by First-Principles Statistical Mechanics, *Phys. Rev. Lett.*, 2004, **93**, 116105.
68 G. Pilania, P.-X. Gao and R. Ramprasad, Establishing the LaMnO3 Surface Phase Diagram in an Oxygen Environment: An *ab Initio* Kinetic Monte Carlo Simulation Study, *J. Phys. Chem. C*, 2012, **116**, 26349–26357.
69 G. Cao, *et al.*, Artificial intelligence for high-throughput discovery of topological insulators: The example of alloyed tetradymites, *Phys. Rev. Mater.*, 2020, **4**, 034204.